An Orientation Measurement Method Based on Hall-effect Sensors for Permanent Magnet Spherical Actuators with 3D Magnet Array

Liang Yan[1,2], Bo Zhu[2], Zongxia Jiao[2], Chin-Yin Chen[3] & I-Ming Chen[4]

[1]School of Automation Science and Electrical Engineering, Beihang University, Beijing, 100191 China, [2]Research Institute of Beihang University in Shenzhen, Shenzhen, 518000 China, [3]Institute of Advanced Manufacturing Technology, Ningbo Institute of Material Technology and Engineering, Ningbo, 315201 China, [4]School of Mechanical and Aerospace Engineering, Nanyang Technological University, 639798 Singapore.

An orientation measurement method based on Hall-effect sensors is proposed for permanent magnet (PM) spherical actuators with three-dimensional (3D) magnet array. As there is no contact between the measurement system and the rotor, this method could effectively avoid friction torque and additional inertial moment existing in conventional approaches. Curved surface fitting method based on exponential approximation is proposed to formulate the magnetic field distribution in 3D space. The comparison with conventional modeling method shows that it helps to improve the model accuracy. The Hall-effect sensors are distributed around the rotor with PM poles to detect the flux density at different points, and thus the rotor orientation can be computed from the measured results and analytical models. Experiments have been conducted on the developed research prototype of the spherical actuator to validate the accuracy of the analytical equations relating the rotor orientation and the value of magnetic flux density. The experimental results show that the proposed method can measure the rotor orientation precisely, and the measurement accuracy could be improved by the novel 3D magnet array. The study result could be used for real-time motion control of PM spherical actuators.

Various working principles have been proposed for displacement measurement of single direction motions[1–7], as well as planar linear motions[8–10]. However, the emergence and development of spherical actuators bring forward the demand of real-time and closed-loop control for multiple degree-of-freedom (DOF) rotational motions in recent years. Detecting the orientation of rotor precisely thus becomes an important research topic for the study of spherical actuators. Quite a few orientation measurement approaches have been proposed by researchers. For example, Lee *et al.* developed a 3-DOF orientation measurement system by utilizing three single-axis encoders to detect the rotor orientation[11,12]. This type of orientation measurement method is capable of achieving high-resolution measurement result. However, it requires two arc-shaped guides and sliding blocks to connect the rotor shaft with the encoders. In this case, there is large friction torque existing on the bearing and sliding blocks, which unavoidably compromises the rotor dynamics and complicates the control implementation. Additional inertial moment is also brought in by the motion of guides. To eliminate this drawback, non-contact sensors are preferred for orientation measurement. A non-contact real-time vision-based orientation measurement system has been proposed by Garner *et al*[13,14]. A spherical shell marked with grid patterns on the surface can be mounted on the rotor shaft. By using imaging processing vision system to capture the grid pattern images, the rotor orientation can be detected. Although there is no contact between the rotor and the measurement system, the surface gridding with high resolution is challenging and the incorporation of image processing module may increase the system size significantly. Lee *et al.* have also proposed another non-contact orientation measurement system by employing optical sensors[15,16]. The operating principle is similar to that of optical mouse. Although the spherical shell with grid patterns is no longer necessary, the output of optical sensor is very sensitive to the gap size between the rotor surface and the sensor tip, and the operation is not very stable. Yan *et al.* also proposed a 3-DOF high-precision non-contact orientation measurement method based on laser detection[17]. By utilizing laser detector to measure the distance between the laser tip and the light spots on a flat plane of the moving body, the orientation of the moving body could be computed. The precision of this

measurement method is impressive, and not affected by gap size. Similarly, the integration into the spherical actuator may increase the system size. Another possible measurement method is Hall-effect sensor. Due to its compact size, it is possible to be integrated into the spherical actuator. The cheap price of Hall-effect sensors also benefits its actual use in future products. Wang *et al.* have used Hall-effect sensors to measure the rotor orientation in spherical actuators[18,19]. Son *et al.* have also employed the similar approach in the spherical wheel motor[20]. Several Hall-effect sensors are placed at different positions surrounding the stator to measure the flux densities. By comparing the measured results with the analytical models of magnetic field distribution, the rotor orientation can thus be obtained. Foggia *et al.* utilized a similar approach to detect the position of bottom aperture of a spherical actuator[21]. Jin *et al.* have demonstrated a method using single Hall-effect sensor to measure the orientation of a non-contact electronic joystick[22]. However, the magnetic field of the rotor with PM poles does not vary too much at certain positions, and thus it is very difficult to detect the rotor orientation in high precision, which constrains the implementation of Hall-effect-based orientation measurement method.

The objective of this paper is to combine novel 3D magnet arrays with Hall-effect sensors, and thus to improve the measurement accuracy of the rotor orientation. The employment of 3D magnet array helps to compensate the variation of magnetic field in 3D space, and thus to increase the measuring resolution. In addition, curved surface fitting method is proposed for the formulation of complex magnetic field in 3D space, to promote the mathematical modeling accuracy. The concept design and poles arrangement of the spherical actuators with 3D magnet array is presented. The magnetic field distribution is then analyzed numerically. A novel distribution of Hall-effect sensors is presented to measure flux density around the rotor. The result is compared with the analytical flux model, and thus to obtain the rotor orientation. Experiments are conducted on research prototype to validate the proposed measurement method. The proposed method could be implemented into other spherical actuators with different pole patterns.

Results

Figure 1 shows the schematic structure of permanent magnet spherical actuator with 3D magnet array. Two Cartesian coordinate systems, XYZ and xyz, are attached on stator and rotor, respectively. They are coincident with each other at the initial position. The motion of rotor can be separated into two steps: 1) the rotor shaft is moved to coincide with desired vector; 2) the rotor rotates about the vector. In this paper, the rotation sequence of the rotor is presented as follows.

- Firstly, frame $\{xyz\}$ rotates about x-axis by an angle of α, and is transformed into frame $\{x_1y_1z_1\}$.
- Secondly, frame $\{x_1y_1z_1\}$ rotates about y_1-axis by an angle of β, and is transformed into frame $\{x_2y_2z_2\}$.
- Lastly, $\{x_2y_2z_2\}$ rotates about z_2-axis by an angle of γ, and is thus transformed into frame $\{x_3y_3z_3\}$.

The direction of rotor's output shaft is determined by two angles, α and β, and spinning angle about the vector is described by γ.

Distribution of Hall-effect sensors. To obtain the analytical solutions of the rotor orientation, Hall-effect sensors are mounted on the stator to detect the magnetic field distribution of the rotor as shown in Figure 2. These sensors point to the sphere center in radial direction. The positions of the sensors are represented with vectors referred in the frame XYZ as

$$Sensor1 : r[\cos \alpha_0 \quad -\sin\alpha_0 \quad 0]^T, Sensor2 : r[\cos \alpha_0 \quad \sin\alpha_0 \quad 0]^T$$

$$Sensor3 : r[-\sin \alpha_1 \quad 0 \quad \cos\alpha_1]^T, Sensor4 : r[\sin \alpha_1 \quad 0 \quad \cos\alpha_1]^T \quad (1)$$

$$Sensor5 : r[0 \quad \cos\alpha_2 \quad -\sin\alpha_2]^T, Sensor6 : r[0 \quad \cos\alpha_2 \quad \sin\alpha_2]^T.$$

where r is the distance from the origin of the coordinate system to the sensors. The positions of these Hall-effect sensors are flexible by changing the values of α_0, α_1, and α_2.

Derivation of orientation. To calculate the rotor orientation, analytical model of magnetic field distribution is important. Two types of magnetic field models are employed for this purpose. One is the conventional magnetic field model based on harmonics expansions, and the other is the curved surface model proposed in this paper.

Derivation of orientation from magnetic field model with harmonics. The modeling process with harmonics expansions of magnetic field
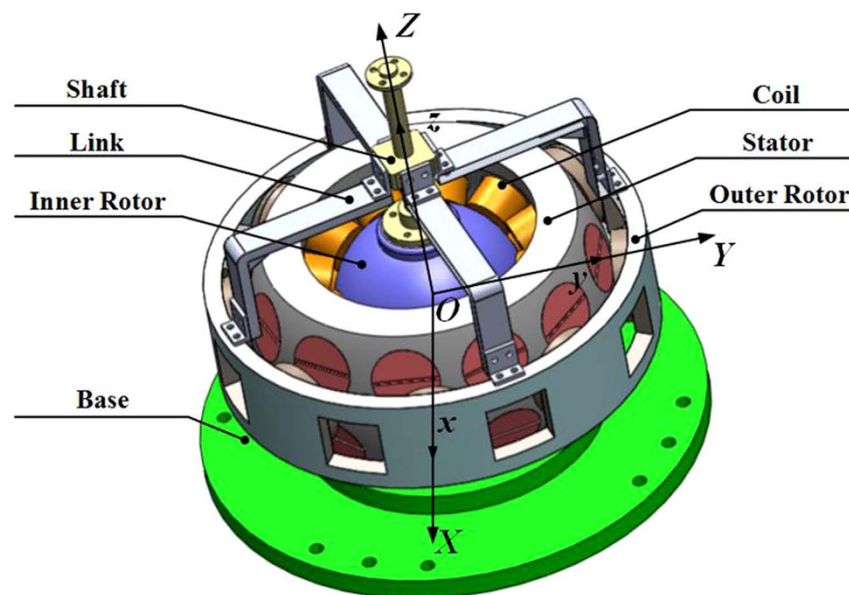

Figure 1 | Concept design and coordinate systems. Twenty four coils are mounted on the stator and symmetrically distributed along the equator. The PM poles are arranged on two rotor surfaces. The inner and outer rotors are fixed together through the L-shaped links. In other words, the magnets are not constrained on a single spherical surface. Instead, they are extended in the radial direction. It helps to improve the torque output and the orientation measurement.
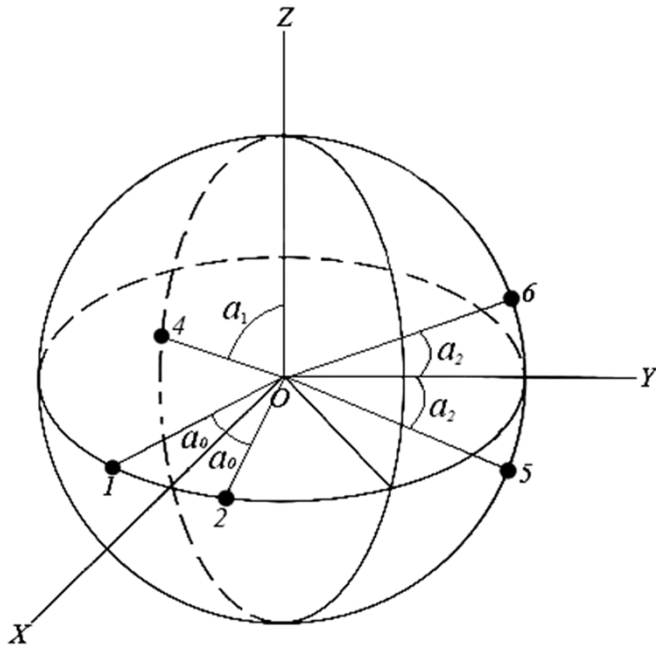
Figure 2 | Distribution of orientation measurement sensors. Sensor 1 and 2 are placed on Plane XY of the stator and α_0 is the angle between the sensor position vector and X-axis. Sensor 3 and 4 are arranged on Plane XZ of the stator and α_1 is the angle between the sensor position vector and Z-axis. Sensor 5 and 6 are placed on Plane YZ of the stator and α_2 is the angle between the sensor position vector and Y-axis.

for spherical actuators can be found in[23,24]. The voltage output of Hall-effect sensors, V_j ($j = 1,2,...,6$), can be generally represented as

$$V_j = K \sum B_{rj}. \tag{2}$$

where K is the sensitivity of Hall-effect sensor and B_{rj} is the radial component of flux density at the position of Hall-effect sensor, contributed by the inner and outer magnets. The output voltage V_j contributed by the magnetic field is represented as

$$V_j = KK_1 \sin^4\theta_j \cos4\varphi_j. \tag{3}$$

where K_1 is a constant associated with the distribution of PM poles, and θ_j, φ_j are spherical coordinates representing the sensor's axis with reference to the moved coordinate system. Substituting the absolute positions of Hall-effect sensors into equation (1) and considering the periodicity of γ and the range of α and β, the analytical expressions of the rotation angles could be obtained as

$$\alpha = \arcsin \frac{\sqrt[4]{\frac{V_6}{KK_1}} - \sqrt[4]{\frac{V_5}{KK_1}}}{2 \sin \alpha_0} \quad \alpha \in \left(-\frac{\pi}{4}, \frac{\pi}{4}\right),$$

$$\beta = \frac{1}{2} \text{sgn}(|V_3| - |V_4|) \arcsin \frac{\sqrt{d - \sqrt{d^2 - e^2}}}{2ab} \quad \beta \in \left(-\frac{\pi}{4}, \frac{\pi}{4}\right),$$

$$\gamma = \begin{cases} \frac{1}{4} \arcsin \frac{FV_1 - DV_2}{KK_1(FE - DG)} & |\gamma| < \frac{\pi}{8} \\ \text{sgn}(V_1)\left[\frac{\pi}{8} + \frac{1}{4} \arcsin \frac{GV_1 - EV_2}{KK_1(FE - DG)}\right] & \frac{\pi}{8} < |\gamma| < \frac{\pi}{4} \end{cases}. \tag{4}$$

where

$$a = \sin\alpha_1, \ b = \cos\alpha \cos\alpha_1, \ c = \sin\alpha \cos\alpha_1, \ d = \frac{V_3 + V_4}{KK_1} + 16c^4,$$

$$e = \frac{V_3 - V_4}{KK_1}$$

$A = \cos\beta \cos\alpha_0$, $B = \cos\alpha \sin\alpha_0$, $C = \sin\alpha\sin \beta\sin\alpha_0$, $D = [(A-C)^2 - B^2]^2 - 4B^2(A-C)^2$, $E = -4B(A - C)[(A - C)^2 - B^2]$,

$$F = [(A+C)^2 - B^2]^2 - 4B^2(A+C)^2. \tag{5}$$

Numerical computation is employed to validate the derived analytical model of rotor orientation. The finite element method (FEM) model and the magnetization patterns of the PM poles are presented in Figure 3. Figure 4 shows the comparisons between analytical and actual rotation angles with 3D magnet array. The red line represents the actual tilting angle in FEM model, whereas the blue line is the tilting angle from analytical model. Relative large difference is
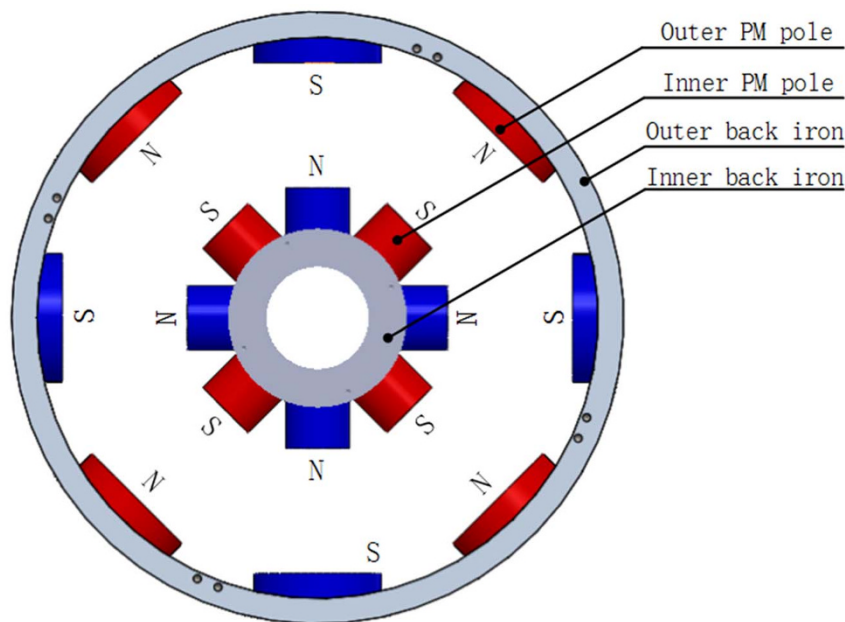

Figure 3 | FEM model of the PM spherical actuator with 3D magnet array. In the analysis, the connection links and housing parts are removed, because they have no significant influence on the magnetic flux distribution.
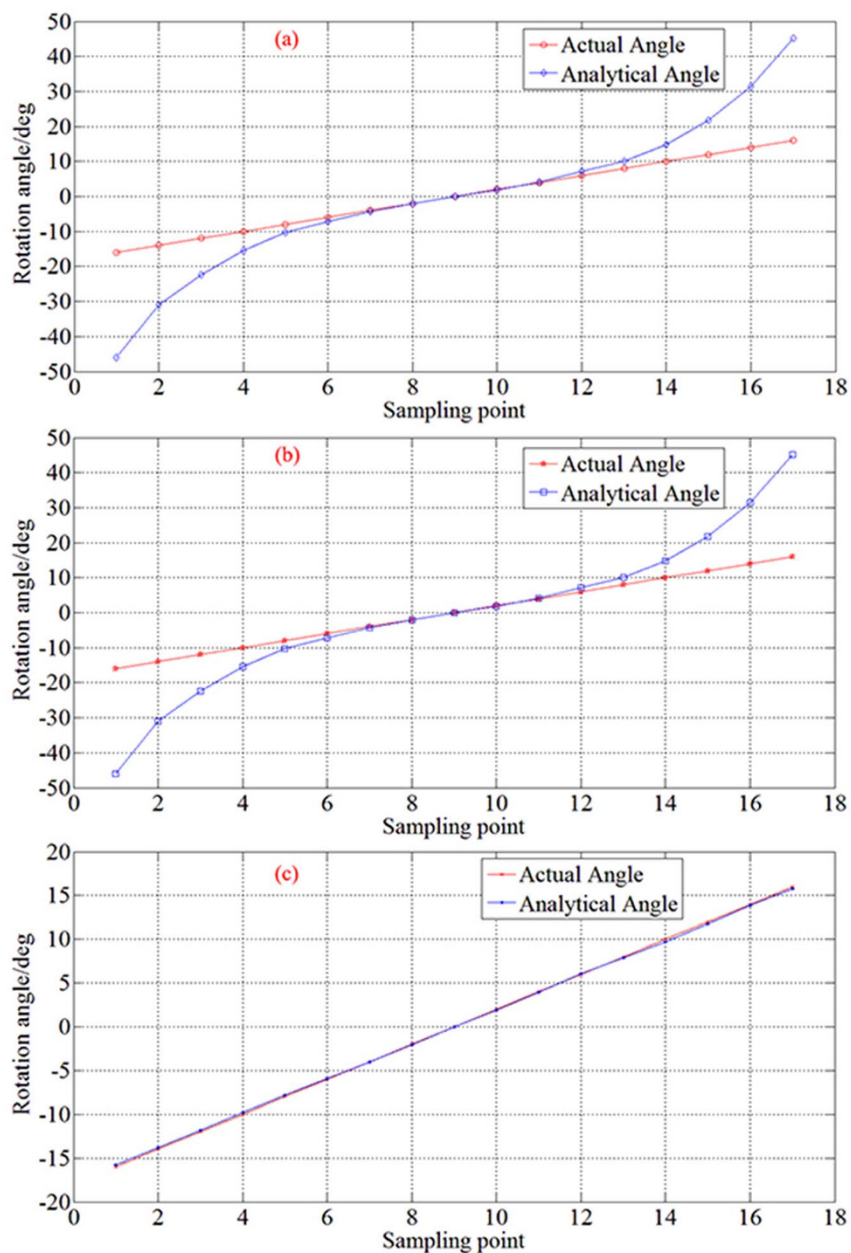
Figure 4 | Comparisons between analytical and actual rotation angles with 3D magnet array. (a) Comparison between analytical and actual rotation angle α. (b) Comparison between analytical and actual rotation angle β. (c) Comparison between analytical and actual rotation angle γ.

observed between the actual and analytical results in Figures 4(a) and (b), which is mainly caused by the simplification of analytical models. However, in Figure 4(c), the analytical model fits with the actual value more closely. The periodical variation of PM poles in the spinning direction may help to improve the precision of analytical models.

Derivation of rotor orientation from curved surface fitting method. To improve the precision of analytical models, curved surface fitting method is proposed to formulate the magnetic field distribution of spherical actuators. Numerical result of the magnetic field distribution of the PM rotor is obtained from Maxwell. It is known that the radial component of magnetic flux density decreases when the concerned point moves away from the rotor equator, and it varies periodically along the rotor equator. Therefore, a hybrid mathematical expression with exponential and trigonometric functions is employed to fit the numerical computations of 3D magnet array as following

$$B_r = 0.159 e^{-\left(\frac{\theta-90}{21}\right)^2} \cos 4\varphi. \tag{6}$$

where θ and φ are the spherical coordinate angles of the position vector referred to the rotated coordinate system. And V_j ($j = 1,2,...,6$) can be expressed as

$$V_j = K B_r = 0.159 K e^{-\left(\frac{\theta-90}{21}\right)^2} \cos 4\varphi. \tag{7}$$

However, from this equation, it is very challenging to derive the analytical solutions of the orientation by using the six Hall-effect sensors at the above-mentioned positions. To obtain the analytical solutions conveniently, two additional Hall-effect sensors are utilized to measure the rotor orientation. The positions of these two sensors are given by
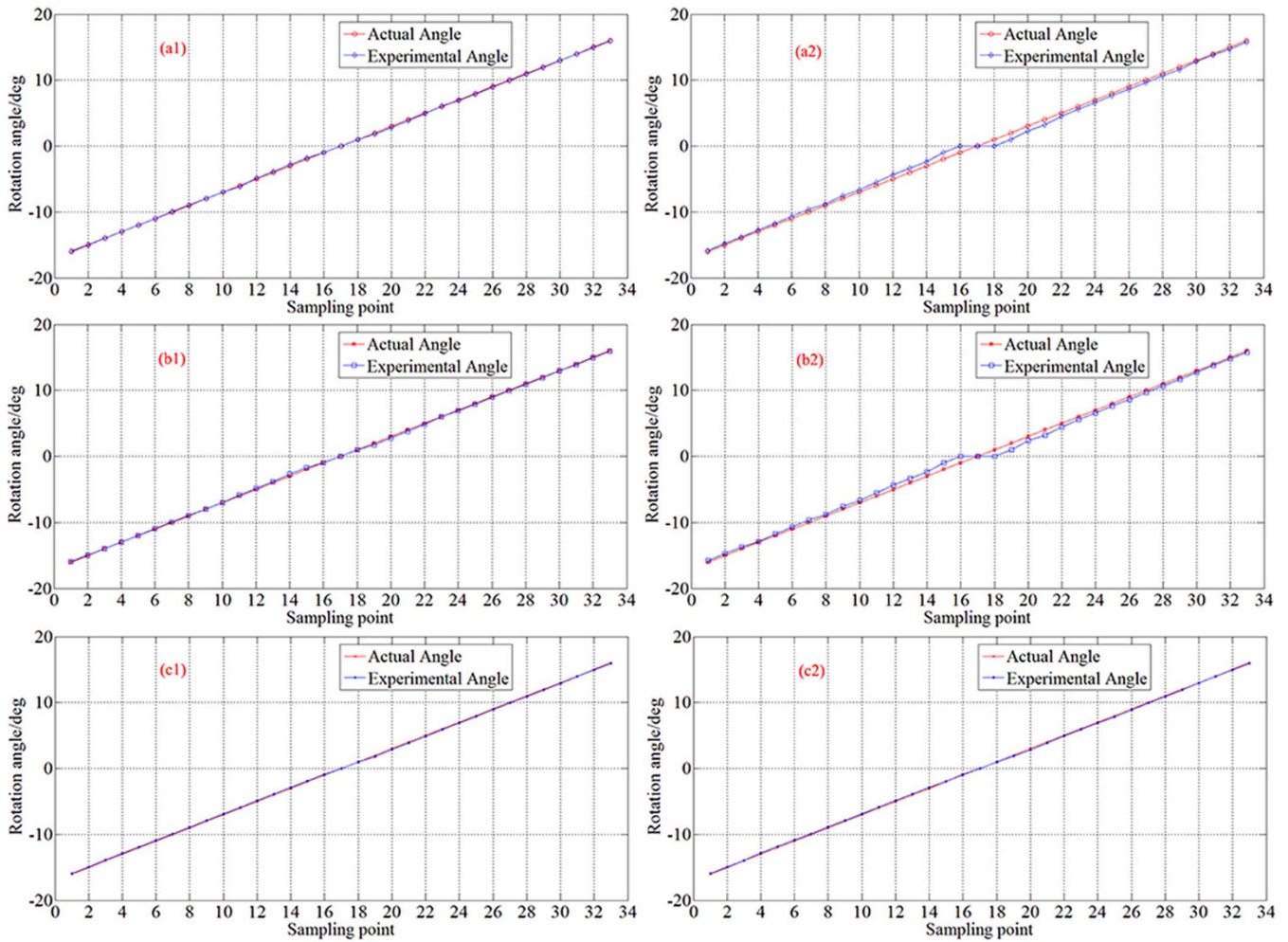
4

Figure 5 | Comparison between the experimental and actual rotation angles with 3D and 2D magnet array. (a1) Comparison between experimental and actual rotation angle α with 3D magnet array. (a2) Comparison between experimental and actual rotation angle α with 2D magnet array. (b1) Comparison between experimental and actual rotation angle β with 3D magnet array. (b2) Comparison between experimental and actual rotation angle β with 2D magnet array. (c1) Comparison between experimental and actual rotation angle γ with 3D magnet array. (c2) Comparison between experimental and actual rotation angle γ with 2D magnet array.

$$Sensor7 : r\begin{bmatrix} 1 & 0 & 0 \end{bmatrix}^T,\ Sensor8 : r\begin{bmatrix} 0 & 1 & 0 \end{bmatrix}^T. \quad (8)$$

The analytical expression of the rotor orientation thus becomes

$$\psi = 21\mathrm{sgn}\left(|V_i| - |V_j|\right)\sqrt{\ln\frac{0.159K}{V_l}}\ \ \psi \in \left(-\frac{\pi}{4}, \frac{\pi}{4}\right),$$

$$\gamma = \frac{1}{4}\arccos\frac{V_7}{0.159K}\ \ \gamma \in \left(0, \frac{\pi}{4}\right). \quad (9)$$

where $\psi = \alpha$ when $i = 5, j = 6, l = 8$, and $\psi = \beta$ when $i = 3, j = 4, l = 7$. Experiments are also conducted on the orientation measurement for spherical actuators with 2D magnet array. The outer rotor in Figure 1 is removed from the system, i.e., the magnet poles are arranged in 2D surface. By using the same approach, the analytical solution of rotor orientation is expressed as

$$\psi = 24\mathrm{sgn}\left(|V_i| - |V_j|\right)\sqrt{\ln\frac{0.05K}{V_l}}\ \ \psi \in \left(-\frac{\pi}{4}, \frac{\pi}{4}\right),$$

$$\gamma = \frac{1}{4}\arccos\frac{V_7}{0.05K}\ \ \gamma \in \left(0, \frac{\pi}{4}\right). \quad (10)$$

The actual rotation angles are compared with those computed from analytical equations with the experimental sensor datum. Figure 5 shows the comparison of α about x-axis, β about y-axis, and γ about z-axis in 3D and 2D magnet array, respectively. The red line represents the tilting angle read from the arc guide, whereas the blue line is the tilting angle from analytical model by experiments. It shows that the employment of 3D magnet array helps to increase the measuring resolution.

Discussion

The maximum difference between actual rotation angles and experimental results for 2D magnet array is about 2°, and 0.5° for 3D magnet array, which indicates that the use of 3D magnet array helps to improve the orientation measurement accuracy of the spherical actuator. To observe the variation of flux density more clearly, the derivative of B_r is taken with respect to the tilting angle. The result is presented in Figure 6. The measurement range of tilting angle for 3D magnet array can be derived from

$$\left|\frac{dB_r}{d\theta}\right| = \left|159e^{-\left(\frac{\theta-90}{21}\right)^2}(-2)\frac{\theta-90}{21^2}\right| < 0.4. \quad (11)$$

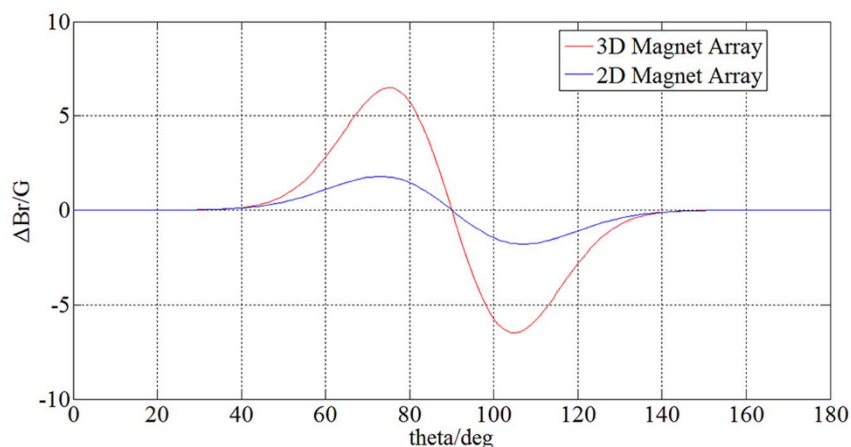**Figure 6 | Derivative of B_r with respect to θ.** The red line shows the derivative of Br with respect to θ of 3D magnet array. And the blue one shows that of 2D magnet array. When θ is equal to 75.1508°, the derivative of B_r with respect to θ of 3D magnet array gets its maximum. To 2D magnet array, the θ is equal to 73.0294°.

Its solution is

$$(46.0936°, 89.4449°) \cup (90.5551°, 133.9064°). \qquad (12)$$

Similarly, the measurement range of 2D magnet array can be derived from

$$\left| \frac{dB_r}{d\theta} \right| = \left| 50 e^{-\left(\frac{\theta-90}{24}\right)^2} (-2) \frac{\theta-90}{24^2} \right| < 0.4. \qquad (13)$$

Its solution is

$$(46.3366°, 87.6743°) \cup (92.3257°, 130.6634°). \qquad (14)$$

Figure 6 shows that the derivative of 3D magnet array is twice larger than that of 2D magnet array when the rotor tilts the same angle, which indicates that the 3D magnet array helps to improve the measurement precision about three times as that of 2D magnet array. The 3D magnet array can also help to improve the measurement range of the tilting angles.

Methods

Experimental apparatus. Experiments are conducted to validate the analytical solution of rotor orientation. Figure 7(a) shows a single converted SS496A Hall-effect sensor that is used in this experiment to measure the magnetic flux density. The integrated circuit in it is apart from the back side about 1 mm, and the inner radium of the stator is 60 mm. Thus, the distance from Hall-effect sensors to the rotor center is about 59 mm. The measurement of the Hall-effect sensor is from −0.8 T to 0.8 T and the sensitivity is 2.5 mV/G. Due to the embedded amplifier, voltage outputted by the Hall-effect sensor is always equal to one half of the supply voltage when there is no magnetic field. So V_j is equal to the absolute value of the discrepancy between the detected voltage and the half of the supply voltage, rather than the voltage detected, i.e.,

$$V_j = \left| V_d - \frac{1}{2} V_s \right|. \qquad (15)$$

where V_d is the voltage detected by the digital multimeter directly and V_s is the voltage supply of Hall-effect sensors. The distribution of Hall-effect sensors is presented in Figure 7(b). It is consistent with that in figure 2. Hall-effect sensors are fixed on the stator and the wires leaded from the pins of each Hall-effect sensor are marked with numbers for distinguishing. Figure 7(c) presents the apparatus for measuring tilting angle. The DC power supply provides the voltage of Hall-effect sensors and the digital multimeter is used to measure the output voltage of Hall-effect sensor when the rotor tilting along the arc guide. The rotor center is coincident with the center of arc guide. Hence, the actual tilting angle of the rotor is indicated by the grids on the arc guide.
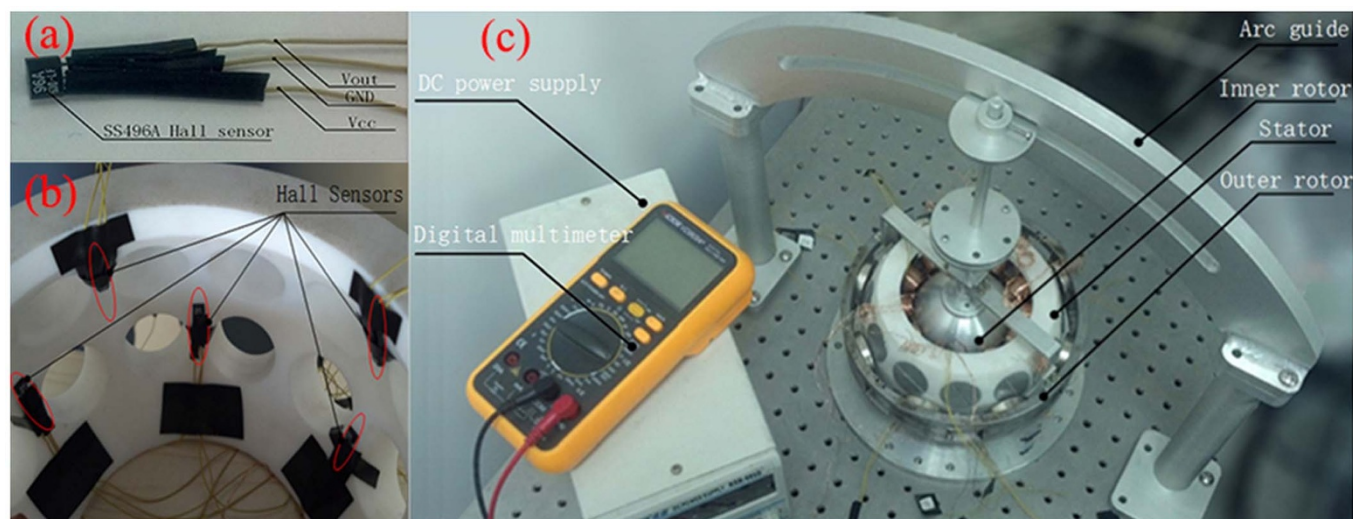

Figure 7 | All apparatuses for measuring tilting angle. (a) The converted SS496A Hall-effect sensor. (b) The distribution of Hall-effect sensors on stator. (c) The test bed for measuring tilting angle.
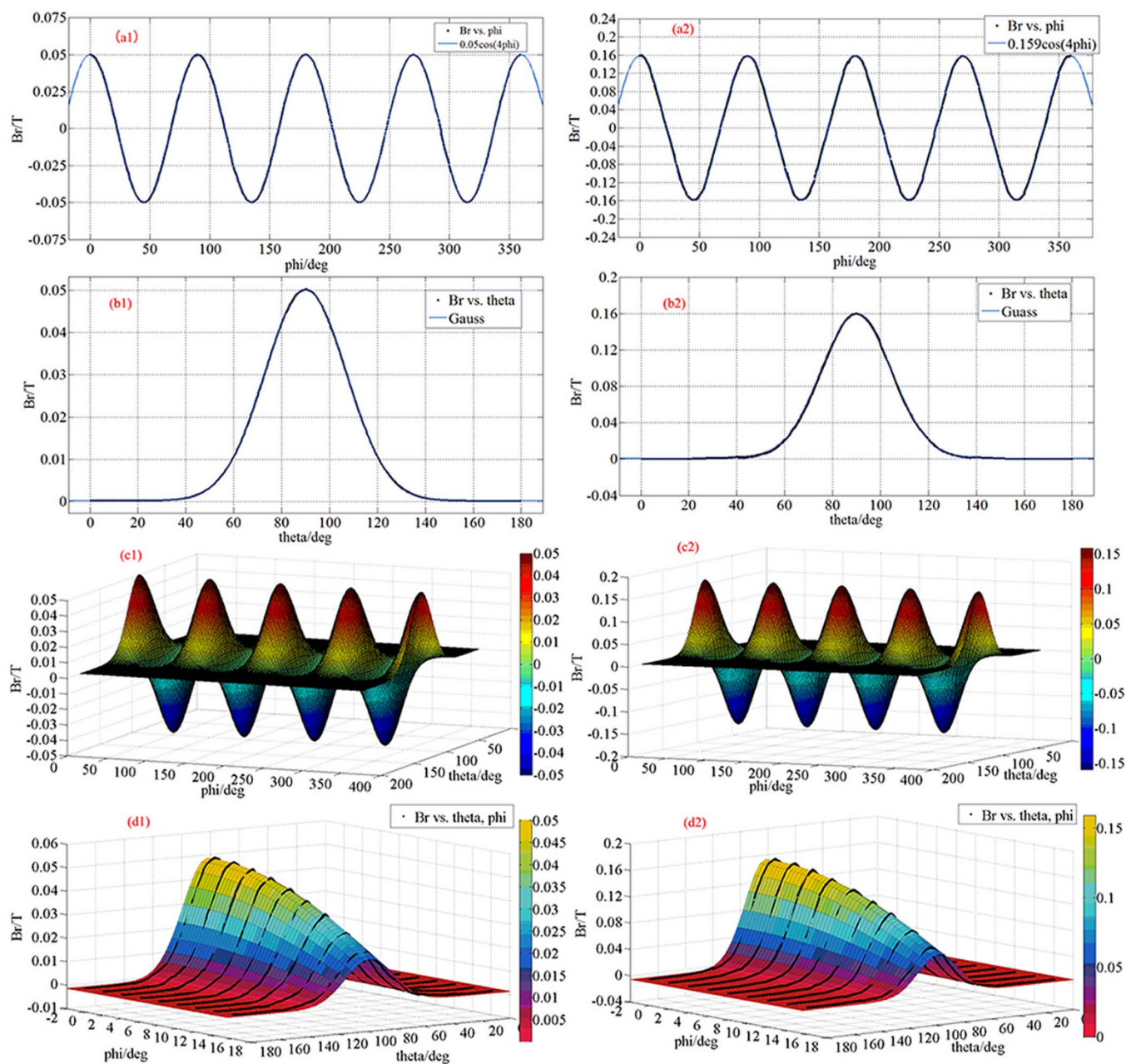
Figure 8 | Curved Surface fitting method for 2D and 3D magnet array. (a1) 2D view of the curved surface fitting @$\theta = 90°$ for 2D magnet array. (a2) 2D view of the curved surface fitting @$\theta = 90°$ for 3D magnet array. (b1) 2D view of the curved surface fitting @$\varphi = 0°$ for 2D magnet array. (b2) 2D view of the curved surface fitting @$\varphi = 0°$ for 3D magnet array. (c1) Complete 3D view of the curved surface fitting for 2D magnet array. (c2) Complete 3D view of the curved surface fitting for 3D magnet array. (d1) 3D detail view of the curved surface fitting for 2D magnet array. (d2) 3D detail view of the curved surface fitting for 3D magnet array.

Curved surface fitting method. Figure 8(a1) and (a2) present the relationship between B_r and φ at $\theta = 90°$. The sampling points from numerical computation are arranged from $0°$ to $360°$ at the step of φ by $0.36°$. Figure 8(b1) and (b2) show the relationship between B_r and θ at $\varphi = 0°$. The sampling points are from $\theta = 0°$ to $180°$ at the step of $\theta = 0.18°$. Figure 8(c1) and (c2) are the 3D views of the curved surface fitting equation for 2D and 3D magnet array. Enlarged views consisting of small parts of the fitting curved surfaces are represented in Figure 8(d1) and (d2) to illustrate more fitting details. They show that the curved surfaces match the numerical results well. Therefore, transcendental equation can be used to describe the distribution of the magnetic field in 3D space.

1. Saxena, S. C. & Sahu, C. Differential inductive ratio transducer with short-circuiting ring for displacement measurement. *IEEE T. Instrum. Meas.* **43**, 777–780 (1994).
2. Dong, L., Nelson, B. J., Fukuda, T. & Arai, F. Towards nanotube linear servomotors. *IEEE T. Autom. Sci. Eng.* **3**, 228–235 (2006).
3. Lee, S. Development of a new variable remote center compliance (vrcc) with modified elastomer shear pad (esp) for robot assembly. *IEEE T. Power. Electr.* **2**, 193–197 (2005).
4. Shan, Y., Speich, J. E. & Leang, K. K. Low-cost IR reflective sensors for submicrolevel position measurement and control. *IEEE/ASME T. Mech.* **13**, 700–709 (2008).
5. Bone, G. M. & Ning, S. Experimental comparison of position tracking control algorithms for pneumatic cylinder actuators. *IEEE/ASME T. Mech.* **12**, 557–561 (2007).
6. Falkner, A. H. The use of capacitance in the measurement of angular and linear displacement. *IEEE T. Instrum. Meas.* **43**, 939–942 (1994).
7. Ferrari, P., Flammini, A., Marioli, D. & Taroni, A. IEEE 1588-based synchronization system for a displacement sensor network. *IEEE T. Instrum. Meas.* **57**, 254–260 (2008).
8. Liu, X., Wang, Y. & Sun, Y. Cell contour tracking and data synchronization for real-time, high-accuracy micropipette aspiration. *IEEE T. Autom. Sci. Eng.* **6**, 536–543 (2009).

9. Xu, Q. S., Li, Y. & Xi, N. Design, fabrication, and visual servo control of an XY parallel micromanipulator with piezo-actuation. *IEEE T. Autom. Sci. Eng.* **6**, 710–719 (2009).

10. Huang, H. *et al.* Visual-based impedance control of out-of-plane cell injection systems. *IEEE T. Autom. Sci. Eng.* **6**, 565–571 (2009).

11. Lee, K. M. & Sosseh, R. A. Effects of fixture dynamics on back-stepping control of a VR spherical motor. *IEEE ICARCV.* **1**, 384–389 (2002).

12. Sosseh, R. A. Finite element torque modeling and back-stepping control of a spherical motor. *Gatech. Ph.D. thesis.* (2001).

13. Harry, D. G. Development of a real-time vision based absolute orientation sensor. *Gatech. Ph.D. thesis.* (2001).

14. Garner, H. & Lee, K. M. Development of a vision based orientation sensor. *ASME IMECE.* **1**, 173–180 (2000).

15. Lee, K. M. & Zhou, D. A spherical encoder for real-time measurements of three-DOF wrist orientations. *Proc. IEEE/RSJ IROS.* **2**, 1596–1601 (1998).

16. Lee, K. M. & Zhou, D. A real-time optical sensor for simultaneous measurement of three-DOF motions. *IEEE/ASME T. Mech.* **9**, 499–507 (2004).

17. Yan, L. *et al.* A three degree-of-freedom optical orientation measurement method for spherical actuator applications. *IEEE T. Autom. Sci. Eng.* **8**, 319–326 (2011).

18. Wang, J., Jewell, G. W. & Howe, D. Analysis, design and control of a novel spherical permanent-magnet actuator. *IEE P-Elect. Pow. Appl.* **145**, 61–71 (1998).

19. Wang, J., Wang, W., Jewell, G. W. & Howe, D. A novel spherical permanent magnet actuator with three degrees-of-freedom. *IEEE T. Magn.* **34**, 2078–2080 (1998).

20. Lee, K. M. & Son, H. Torque model for design and control of a spherical wheel motor. *IEEE/ASME ICAIM.* **1**, 335–340 (2005).

21. Foggia, A., Olivier, E., Chappuis, F. & Sabonnadiere, J. A new three degrees of freedom electromagnetic actuator. *IEEE IAS.* **35**, 137–141 (1998).

22. Jin, H., Lu, H., Cho, S. & Lee, J. Nonlinear compensation of a new noncontact joystick using the universal joint mechanism. *IEEE/ASME T. Mech.* **12**, 549–556 (2007).

23. Yan, L., Chen, I. M., Yang, G. & Lee, K. M. Analytical and experimental investigation on the magnetic field and torque of a permanent magnet spherical actuator. *IEEE/ASME T. Mech.* **11**, 409–419 (2006).

24. Yan, L. *et al.* Design, modeling and experiments of 3-DOF electromagnetic spherical actuators. *Springer.* (2011).

Acknowledgments

Author contributions

L.Y. is the principal investigator who proposed and organized the study. B.Z. analyzed the rotation measurement. L.Y. and B.Z. wrote the main manuscript text and prepared Figures 1–8. Z.X.J., C.Y.C. and I.M.C. reviewed the manuscript and gave some critical suggestions.

Additional information